Validation of a High-Order Implicit LES Solver Using a NACA0012 Airfoil and a Low-Re Vertical-Axis Wind Turbine

Samuel Kanner[1] and Per-Olof Persson[2]
University of California Berkeley, Berkeley, CA, 94720

A high-order Implicit Large Eddy Simulations (ILES) method in 2D and 3D is used to simulate the aerodynamics of a NACA0012 airfoil over large angles of attack at low chord Reynolds numbers ($Re = 5,000 - 50,000$). The 2D code is found to have good agreement with lift and drag experimental data for pre-stall angles of attack, while the 3D code is found to have good agreement over all angles of attack. The method is able to accurately predict the magnitude and frequency content of the lift and drag forces on the airfoil throughout the range of Re considered in this study. Further comparisons to experimental data are made, including PIV vorticity data as well as dye-injection data. As an extension of this application, a section of a constant spinning straight-bladed vertical-axis wind turbine with two blades at a similar Re is subject to various inflow velocities in 2D and 3D. The pitch angle of the blades was also varied in order to take into account the uncertainties in the mounting angle of the blade in the experimental studies. As found previously, a small toe-out angle can increase the power absorption of the turbine on the order of 10%. The computed tangential forces as a function of the azimuthal angle agree much better to the experimental data at high tip-speed ratios as compared to other, lower-fidelity analytical turbine codes.

[1] Ph.D. Candidate, Department of Mechanical Engineering, University of California Berkeley, Berkeley CA 94720. E-mail: kanners@berkeley.edu. AIAA Student Member.
[2] Associate Professor, Department of Mathematics, University of California Berkeley, Berkeley CA 94720-3840. E-mail: persson@berkeley.edu. AIAA Senior Member.

Nomenclature

Roman Characters

A_v	Swept area of VAWT
c	Chord length of VAWT blade
c_0	Distance from LE along chord line of mount point
C_D	Sectional airfoil drag coefficient, $2F_D/(\rho U_\infty^2 c)$
C_L	Sectional airfoil lift coefficient, $2F_L/(\rho U_\infty^2 c)$
C_p	Sectional power coefficient of turbine, $2P/(\rho U_\infty^3 A_v)$
C_T	Sectional VAWT tangential force coefficient, $2F_T/(\rho U_\infty^2 c)$
H	Vertical height of VAWT blade
N_b	Number of VAWT blades
R	VAWT radius at equator
Re	Chord Reynolds number, $\rho U_\infty c/\mu$
t^*	Normalized time, tU/c
U_∞	Free-stream horizontal fluid velocity

Greek Symbols

α	Angle of attack of airfoil
α_0	Preset pitch angle of airfoil
λ	Tip-speed ratio of VAWT, $\mathrm{R}\omega/U_\infty$
ω	Angular velocity of VAWT rotor

I. Introduction

Throughout the 1970s and into the 1980s, Sandia National Laboratories conducted research into the design and testing of vertical-axis wind turbines (VAWTs). At that time, the nascent wind energy industry had not converged on a single optimal design, such as the three-bladed upwind horizontal-axis seen widely today. Recently, however, there has been renewed interest in commercializing VAWTs, especially in an offshore setting. Due to their lower center of gravity and more accessible electromechanical components, VAWTs could be a superior technology over HAWTs on a floating platform. Their use in a floating environment could result in lower capital costs (due to the smaller platform) as well as operational and maintenance costs. Though only a few large-scale prototypes of floating wind turbines exist today (see, for instance [1]), many developed countries have a large untapped offshore wind resource in deep water (usually defined as greater than 50m water depth), such as the U.S., U.K., China, Japan, and many others. However, the design, manufacture, and maintenance of even a large-scale *onshore* VAWT has proven to be difficult due to the lack of available accurate data (numerical or experimental) on the magnitude and frequency content of the instantaneous aerodynamic forces on the blades [2]. Further, nearly all analytical models used to model VAWTs require some experimental data in their analysis.

One challenge to predicting forces on a VAWT blade is the large variation in angle of attack of the airfoil as it circumnavigates the central column. At certain tip-speed ratios, namely $\lambda \geq 5$, the angle of attack does not exceed $12°$, as depicted in Fig. 10. Previous researchers [3–5] have found that three-dimensional Large Eddy Simulation (LES) [6] is necessary to accurately predict the lift and drag of a stalled airfoil. At the lowest TSR ($\lambda \leq 1$), Li *et al* [5] showed that 3D LES (this form of LES is sometimes called 2.5D LES) could accurately predict the tangential force of a straight-bladed VAWT at $Re = 10^5$. However at higher TSR ($1.4 \leq \lambda \leq 2$, the 3D LES model could not accurately predict the forces, especially in the downwind section. For all λ studied in [5], the maximum tangential forces computed by the 3D URANS simulations were nearly a factor of 2 above the experiments. Though 3D large-eddy simulations (LES) will always exhibit higher fidelity than 2D simulations, the computational cost of such a simulation may be prohibitive. For $\lambda \geq 5$, however, it remains to be determined whether a 2D simulation of a VAWT can accurately predict the forces.

Although the ILES methodology used in the present study only exhibits adequate stability and robustness properties for $Re < 10^5$, this methodology can still accurately be applied to the unsteady aerodynamics of airfoils with conditions applicable to micro-air vehicles [7] as well as some model-scale VAWTs. For instance, the Reynolds number of the model turbine tested at the Sandia National Labs tow tank is $\approx 50 \cdot 10^3$ [8]. However, as Lissaman points out in [9], lower Reynolds experiments (defined usually as $10^3 \leq Re \leq 10^5$) even for single airfoils are difficult to perform and repeat. Carmichael [10] also reexamined many low Re wind tunnel airfoil data and found only a few to be reliable. Most wind tunnels have to deal with turbulence effects, wall effects and a wide range of forces present in the experiments which all lead to discrepancies in reported values for similar tests. Thus, many researchers have turned to increasingly higher fidelity numerical methods in order to fully understand the flow features past airfoils or VAWT blades.

The computational efficiency and accuracy of computational fluid dynamics (CFD) simulations have increased dramatically over the past decades. The most common types of simulations, including those found in OpenFOAM, a popular open-source CFD software, are 2D unsteady Reynolds-averaged numerical simulations (URANS). However, these simulations have been found to overestimate the power coefficients of VAWTs due to their delay of the onset of dynamic stall and the overprediction of the tangential force in the upwind zones [5]. In this study, we propose using a high-order ILES method, developed in [11] for a straight-bladed VAWT. To our knowledge, this is the first study of a high-order ILES code being applied to a VAWT either in 2D or 3D. This methodology can convect the vortices that are created by the VAWT blade in the upwind zone into the downwind zone and accurately simulate the effect of these vortices on a moving blade. Though the present study focuses on VAWTs, these lower-Reynolds results can be used for a variety of new applications, such as unmanned-air vehicles, micro-air vehicles, and the simulation of avian and insect flight.

The paper is organized as follows. First, we simulate the flow field about a single static NACA0012 airfoil over a large variation in angle of attack in 2D and 3D. By comparing these simulations to recent experimental data, we determine the range of angle of attack the 2D simulations are valid. We also simulate these airfoils in 3D and compare the frequency content of the forces to experimental data. Then, we numerically recreate the 2-bladed VAWT tested by Strickland in [8] to compare the tangential forces on the VAWT blades in 2D and 3D. Like Li in [5], we found that although 2D LES drastically overpredicted the lift and drag coefficients at post-stall angle of attacks, the fidelity of the VAWT simulation did not suffer over a range of TSR. Indeed, we were able to accurately simulate the forces on the VAWT blade in the upwind and downwind zones. Further, we found that the 2D results generally agreed with the 3D results, especially at high tip-speed-ratios.

II. Governing Equations and High-Order Discontinuous Galerkin Discretization

Our simulations are based on the Navier-Stokes equations, and we use an artificial compressibility method based on an isentropic formulation [12] to approximate the nearly incompressible flows that we are modeling. This results in a system of equations in the conserved variables ρ (density) and $\rho\boldsymbol{u}$ (momentum). We impose two types of boundary conditions, free-stream flow (far field) and zero velocity (wall).

The equations are discretized using a high-order Discontinuous Galerkin (DG) formulation. While not used routinely for CFD simulations, high order methods have been shown to be advantageous for applications requiring low numerical dispersion and high time accuracy [13]. In particular, they are believed to produce reliable results already on coarse grids for LES simulations with highly separated flows [11].

We use an in-house developed code for the simulations, which uses high-order DG methods on fully unstructured meshes of tetrahedral elements and nodal basis functions [14, 15]. The DG method produces stable discretizations of the convective operator for any order discretization, thus avoiding the need for additional stabilization or filtering. Here, we use polynomial degrees $p = 3$ for all the simulations, which is commonly considered a good compromise between high order accuracy and increased solver cost. The viscous terms are discretized using the Compact Discontinuous Galerkin (CDG) method [16] which leads to optimal order accuracy, is compact, and generates sparser matrices than the alternative existing methods. For the time-integration, we use a 3-stage, 3rd order accurate Diagonally Implicit Runge-Kutta (DIRK) method.

For the turbine simulations, we account for the moving and deforming domains by the mapping based Arbitrary Lagrangian-Eulerian (ALE) formulation proposed in [14]. It is accurate to arbitrary orders in both space and time. The so-called Geometric Conservation Law (GCL) is satisfied using an additional equation that is used to compensate for numerical integration errors. The formulation requires that the deformations are prescribed either explicitly or indirectly as a mapping $x = x(X, t)$ between the reference and the physical space. In our case, we can simply use a rotating framework to model the spinning turbine. We can then analytically compute the deformation gradient $\partial x/\partial X$ and the grid velocity $\partial x/\partial t$, and formulate the ALE equations directly in the reference domain. For details on this procedure, see [14].

All triangular and tetrahedral meshes we use are produced using the DistMesh mesh generator [17]. We use a structured approach for the boundary layers around the airfoils, and the 3D meshes are obtained by prismatic extrusion of the triangular elements. In addition, high-order methods require meshes with curved elements, which are particularly difficult to general for meshes with boundary layers. We use the elasticity-based approach proposed in [18], which tends to produce well-shaped meshes with globally curved elements.

III. ILES Simulation of NACA0012 Airfoil

The airflow over streamlined bodies at low to moderately low Re (i.e., $10^3 \leq Re \leq 10^5$) has been examined thoroughly by means of experimental, analytical and computational techniques by many researchers in the modern era (see review papers, for instance, [7, 9, 10, 19]). This Re range presents unique challenges to researchers who have to deal with separated, highly unsteady transitional flow. Though early wind tunnel tests of the NACA0012 were plagued by inaccuracies [20], many recent experimental studies have used state-of-the-art pressure and force measurements as well as flow visualization techniques (see, for instance, [21–25]).

However, experimental studies will always be limited by the amount and type of data that can possibly be collected from such tests. Recent growth in computational power and parallel computing techniques has led to increasingly higher-fidelity computational analyses, such as large-eddy simulation (LES) and direct numerical simulation (DNS), (see [4, 6, 11, 26–32]). While DNS can solve for the flow field at Kolmogorov scales, it requires prohibitively fine meshes for the Reynolds numbers considered, even for high-performance computers. Thus, researchers are actively seeking numerical schemes that could model the flow structures at a wide range of spatial and temporal scales and could accurately predict the magnitude and frequency of forces on the airfoil with lower computational cost. In LES simulations, element sizes are significantly larger than the Kolmogorov scale. This reduces the computational cost drastically, and the effect of the unresolved scales are incorporated through subgrid models. In our work, we use the so-called implicit LES (ILES) model which assumes that this subgrid model is the inherent dissipation of the numerical scheme. In most cases these flow structures are inherently three-dimensional and require full 3D simulation techniques, although in this work we will compare the 3D results with corresponding 2D simulations to highlight the differences.

A. Computational Domain

The airfoil is a standard NACA0012 section, and we use an outer box of size three chord lengths above, below, and upstream from the airfoil, and five chord lengths in the wake. Three different meshes are generated for the simulations, two triangular 2D meshes and one tetrahedral 3D mesh, see figure 1.

The 2D meshes have 1,368 and 7,774 high-order elements, respectively, corresponding to 13,680 and 77,740 high-order nodes, or about 41,000 and 230,000 degrees of freedom. We measure the resolution length of the first layer of elements around the airfoil by dividing the element height by the polynomial degree, $h_{\min}/p$, which is a natural choice for high-order methods. For our two meshes this quantity is $5 \cdot 10^{-4}$ and $5 \cdot 10^{-5}$, respectively.

For the 3D domain, we extrude the 2D airfoil section to a span length of 0.4 chord lengths, and use periodic conditions between the two ends. This leads to a mesh with 151,392 high-order tetrahedral elements, or about 3 million high-order nodes, which correspond to above 12 million degrees of freedom. The first layer of elements has $h_{\min}/p = 2.5 \cdot 10^{-4}$.

B. Results And Discussion

The forces on a stationary NACA0012 airfoil over a range of angles of attack ($0° \leq \alpha \leq 55°$) were obtained and decomposed into the stream-wise and cross-stream directions (F_D and F_L, respectively). These results were compared to experimental and computational data from a variety of previous studies at similar Re. Only recently, as modern sensing technology has advanced, have experimentalists been able to accurately describe the frequency content of the the measured force signal. In the following sections we compare the *magnitude* as well as the *frequency* of the lift and drag forces on the stationary airfoil.

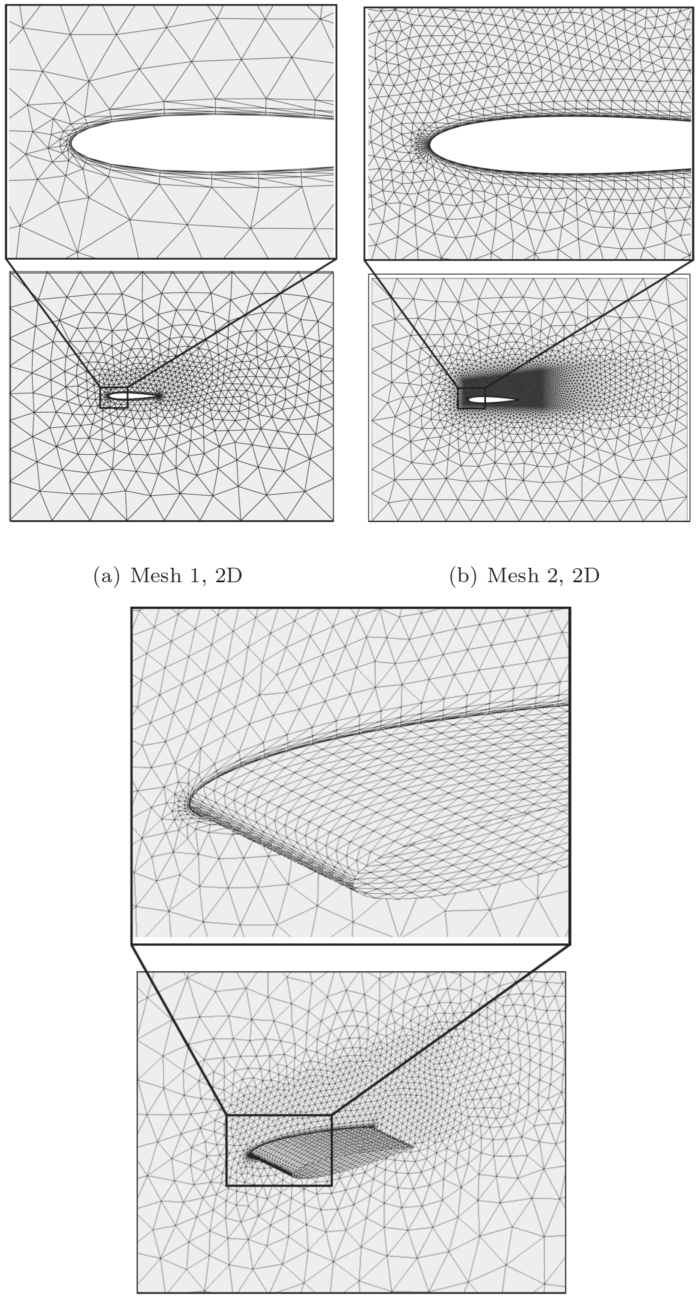

(a) Mesh 1, 2D (b) Mesh 2, 2D

(c) 3D Mesh

Fig. 1 Computational domain in 2D and 3D for the static NACA0012 airfoil at a wide range of angles of attack.

1. Magnitude of Force

The lift coefficients from a variety of experiments and numerical simulations at low Re (5,300 $\leq Re \leq$ 20,700) are shown in Fig. 2. The rectangular box is amplified and shown in Fig. 2(b). The 2D results from the present simulation are displayed with open and filled circles for Mesh 1 and Mesh

2, respectively (no appreciable difference at this level). Experimental data from Alam *et al* [23] are shown in open and filled red diamonds, from Ohtake [25] in blue squares and from Laitone [33] in upside-down green triangles. Many different high-quality experimental tests are shown in these figures due to the difficult nature of obtaining reliable results at such Re. Results from the inviscid linear-vorticity panel method code XFoil [34] are also plotted for comparison. At this Reynolds number, the 2D ILES predicts the lift coefficient of the NACA0012 fairly well up to about α=8°. Above this α the 2D ILES drastically overpredicts the lift force. The XFoil code, however, captures the relatively linear behavior of this airfoil over a larger range, though underpredicts the lift from $3° \leq \alpha \leq 12°$ as shown in Fig. 2(b). The 3D ILES simulations at α= 10°, 12°, 15° and 30° are close to the experimental data. Interestingly, the value at α= 10° is close to the values obtained by XFoil, though the computational cost of obtaining such a datum are orders of magnitude higher for the CFD software compared to the potential flow solver.

The lift coefficients for the NACA0012 at higher Re ($40.0 \cdot 10^3 \leq Re \leq 360 \cdot 10^3$) are shown in Fig. 3 up to α=55° and up to α=12° in Fig. 3(b). The results show similar trends to the ones described in Fig. 2, with the 2D ILES simulations overpredicting the lift values at $\alpha > 10°$. Experimental data from Huang & Lee [35] are shown with grey filled triangles while the data from Sheldahl and Klimas' seminal airfoil testing [36] at large angle of attacks are displayed with cyan triangles. The LES simulations performed by Lehmkuhl, documented in [26] are shown with asterisks in Fig. 3(b). Again, the XFoil code, captures the behavior of this airfoil fairly well. The 3D ILES simulations at 30° and 50° are close to the experimental data. The drag coefficients for NACA0012 at $5 \cdot 10^3 \leq Re \leq 360 \cdot 10^3$ are shown in Fig. 4(a) for $\alpha \leq 55°$ and for $\alpha \leq 12°$ in Fig. 4(b). The trend of increasing Re coinciding with decreasing $C_D(\alpha = 0)$ was shown experimentally in [36]. Both XFoil and the ILES simulations follow the experimental data well for $\alpha \leq 12°$. A similar LES simulation was run for NACA0012 by Pagnutti [37] for $\alpha = 0$, shown with a '+' marker. The drag coefficient coincides exactly with the simulations performed in this study at $C_D = .55$ and the marker is partially obscured in Fig. 4(b). The 3D simulations also provide accurate results under post-stall conditions.

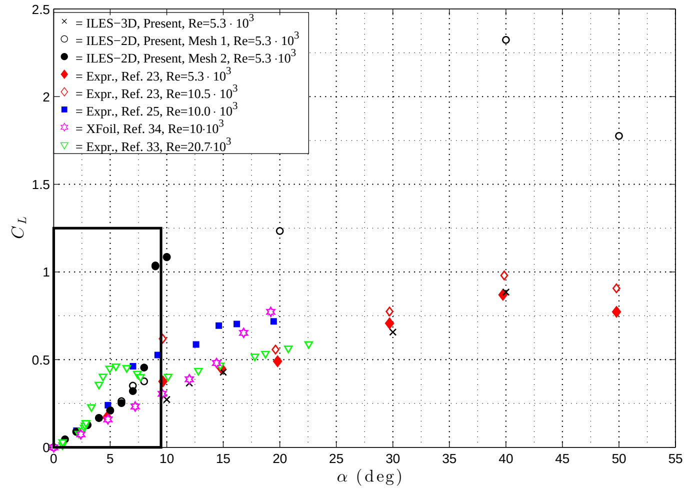

(a) Lift coefficient at large angle of attack.

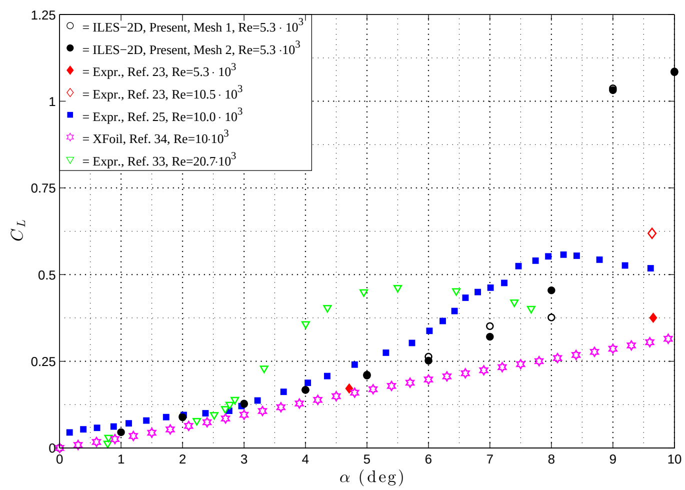

(b) Lift coefficient at small angle of attack.

Fig. 2 Lift coefficient of NACA 0012 at 5,300 $\leq Re \leq$ 20,700.

2. Frequency Content of Force

In order to analyze the frequency content of the ILES simulations, a Fourier transform could be used to analyze the time history of the lift and drag forces. However, since the total simulation time was never greater than 80 s due to time and storage constraints, a desired frequency resolution of 0.01 Hz could not be obtained. Thus, the peaks of the signals were obtained by finding the zero-slope and the dominant frequency of the lift force was obtained through the averaging of these periods. The data obtained from this procedure are shown in Fig. 5. These results are compared to the dominant frequencies in the lift signal experimentally determined by Alam in [23]. They are also compared to dominant vortex shedding frequencies found in the DNS simulations of a NACA0012

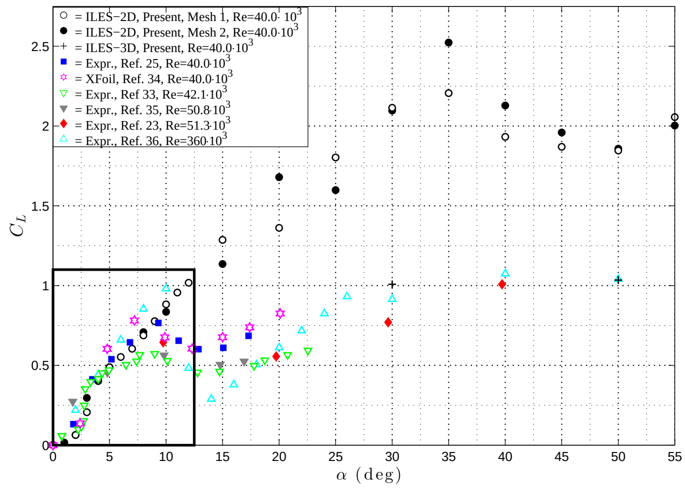

(a) Lift coefficient at large angle of attack.

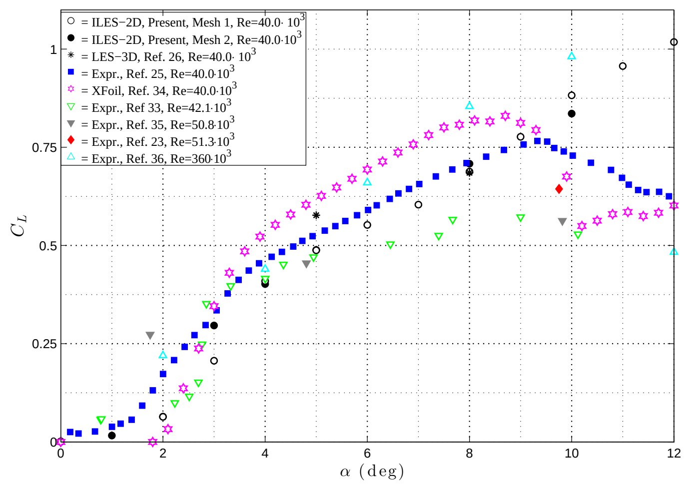

(b) Lift coefficient at small angle of attack.

Fig. 3 Lift coefficient of NACA 0012 at Re 40,000 and above.

at $\alpha = 9.25, 12$ by Rodriguez in [32] as well as the dominant vortex shedding frequencies found in the experiments performed by Huang and reported in [22]. In the literature, when the frequency of the vortex-shedding is discussed, the length scale is generally related to the width of the wake. However, these aforementioned authors use slightly different length scales for the length parameter of the Strouhal number. To simplify, we just use the chord length c. From the agreement in Fig. 5 over the large range of angles of attack, it is evident that the oscillations in the force signal are due to the shedding vortices. The dominant frequencies in the drag force were similar to those of the lift force as experimentally determined in [23] and are not reproduced here.

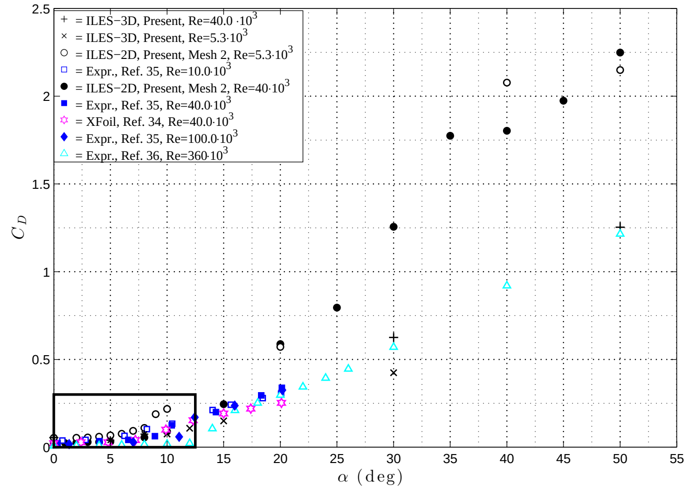

(a) Drag coefficient at large angle of attack.

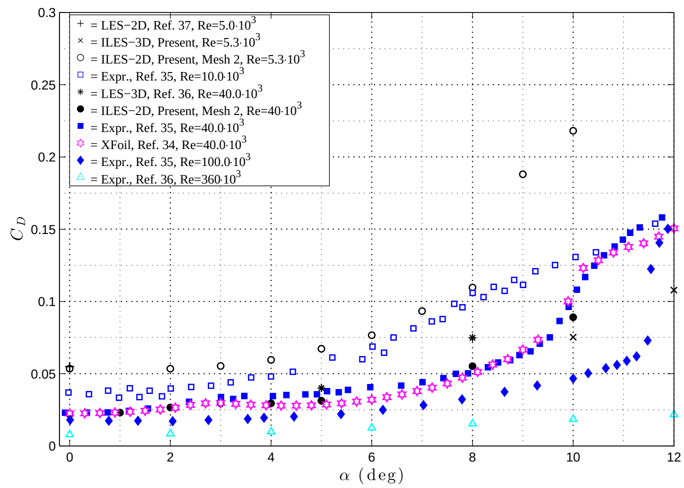

(b) Drag coefficient at small angle of attack.

Fig. 4 Drag coefficient of NACA 0012 at $5 \cdot 10^3 \leq Re \leq 360 \cdot 10^3$.

C. Flow Structure

To analyze the fidelity of the unsteady flow structures in the 3D ILES simulation, two comparisons with experimental data were performed: the first was with a dye injection the second was with interpolated PIV data.

1. *Dye-Injection*

In the experiments reported in [23], flow visualization was performed using a dye-injection technique. The dye was injected with a 1 mm nozzle at three different sites along the midspan of the airfoil: the nose of the airfoil and 0.1 chord lengths from the nose on the suction and pressure

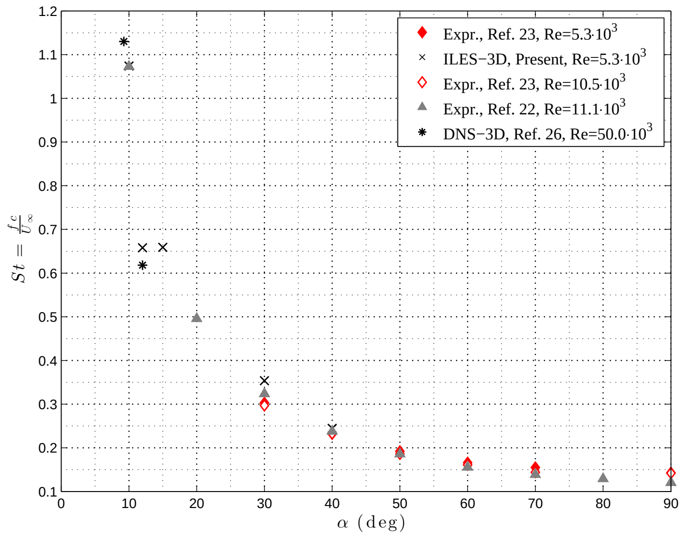

Fig. 5 Comparison of dominant non-dimensional frequencies, fc/U_∞, of lift force or vortex shedding over a large range of angle of attack at low Re.

sides of the airfoil. To compare with the images from this study, a particle-tracing algorithm in the ParaView visualization software [38] was employed. In the particle-tracer simulation, only the nose and suction side injection sites were chosen to minimize computation time. One instant of this simulation ($t^* = 4.05$) is shown for $\alpha = 10°$ and $Re = 5.3 \cdot 10^3$ in side view in Fig. 6 and compared to the image shown in [23] for the same flow parameters. Although the particle-tracer

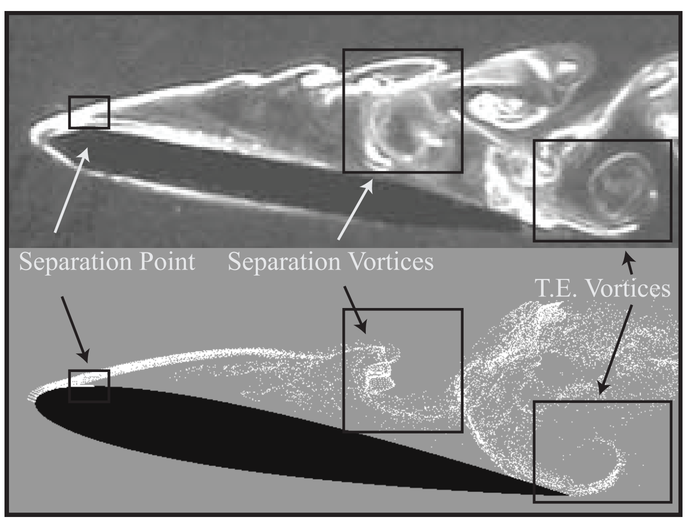

Fig. 6 Comparison of dye-injection visualization experiment at $\alpha = 10°$ and $Re = 5.3 \cdot 10^3$ (from [23]) and particle-tracer post-processing from 3D ILES simulation.

technique neither includes the effect of the input velocity of the dye nor its diffusion properties, the images show relatively good agreement. Although it is not possible to see the time evolution of the vortical structures in this particle tracer simulation, the flow structures are similar to the ones in 'Regime C' that Huang describes in [21]. As the separation point moves upstream, a surface vortex is formed in the separated boundary layer around the mid-chord. As the counter-clockwise rotating vortex rolls down the suction side of the airfoil and is shed into the surround fluid, a trailing-edge vortex (clockwise-rotating) rolls up from the pressure side to the suction side. Huang attributes this effect to the low pressure region immediately behind the counter-clockwise rotating vortex. The vortices are shed in an alternating fashion, with a counter-clockwise rotating one generated from the trailing-edge and clockwise-rotating generated in the separated boundary region and rolling down the suction side of the airfoil.

2. *Vorticity PIV Data*

In [21], Huang and colleagues impulsively started a NACA0012 airfoil at various angles of attack in a water tank. The PIV images were obtained from a CCD camera that was mounted on a small moving carriage below the tank (see Fig. 1 in [21] for experimental setup). The water was seeded with polyamide particles to reflect the laser light and the airfoil was towed such that $Re = 1.2 \cdot 10^3$. Once the original velocity field was calculated from the PIV data, the data were enhanced by interpolating at points with a weighting distance of $1/r^2$. The vorticity was calculated from a central difference scheme from this interpolated data. These contours with labels showing the magnitude of the vorticity are shown in black in Fig. 7. This data is superimposed with the colored filled contour data from the midspan of the 3D ILES simulations at $Re = 5.3 \cdot 10^3$. The results show remarkably good agreement for the spatial and temporal evolution of the vortical structures despite the different flow parameters ($Re = 1.2 \cdot 10^3$ versus $Re = 5.3 \cdot 10^3$). As Huang describes in [21], at this large angle of attack, a starting vortex is generated from the leading-edge ($t^* < 1.0$). As this vortex rolls down the suction side of the airfoil ($1 < t^* < 2.67$), it induces a trailing-edge vortex in its stead (much like the evolution described in Sec. III C 2 at lower α). Eventually this leads to alternative shedding of a surface vortex and trailing-edge vortex.

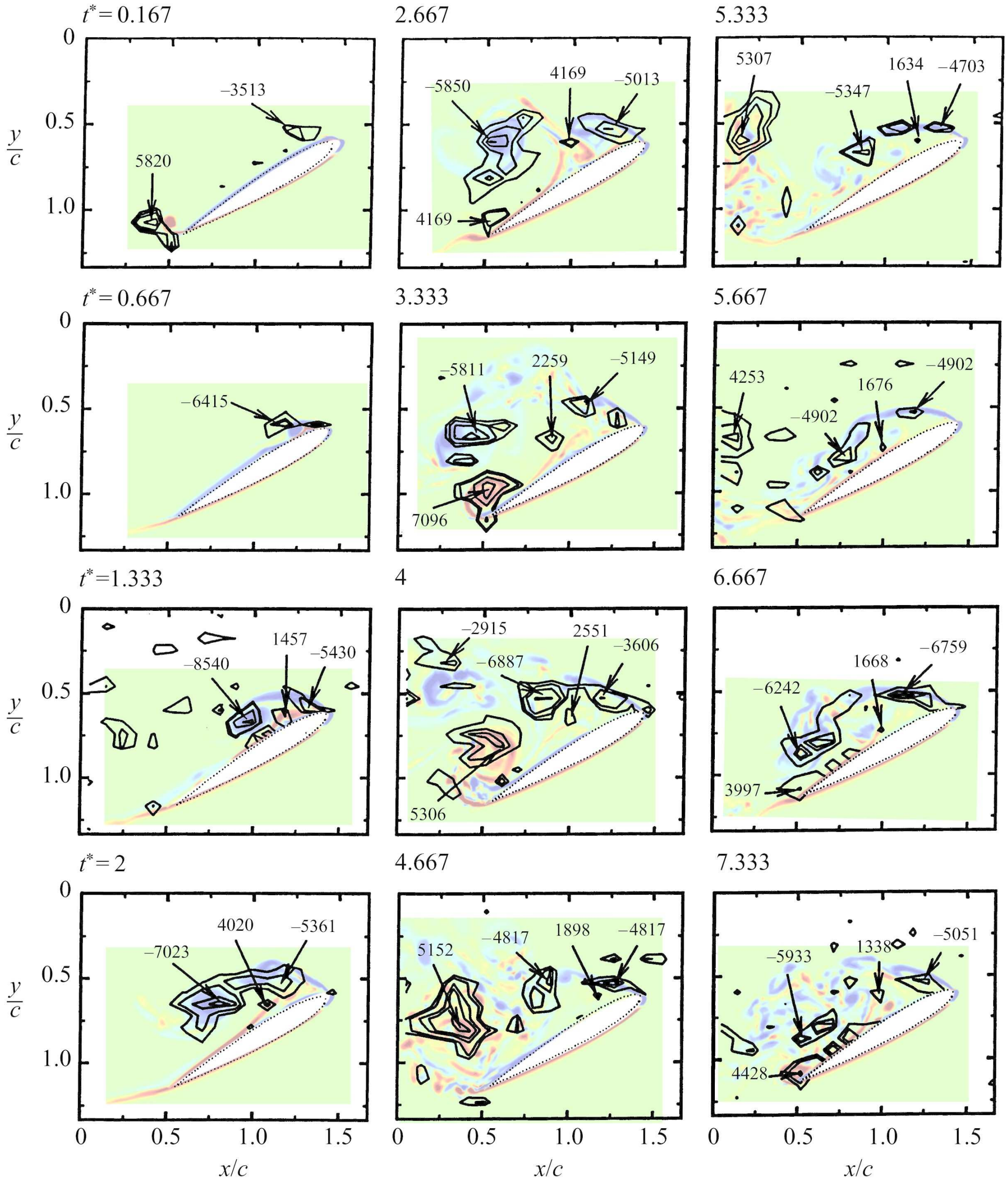

Fig. 7 Comparison of vorticity at various normalized time instances, at $\alpha = 30°$ from interpolated PIV data (Fig. 14 from [21]) at $Re = 1.2 \cdot 10^3$ in black contours and labels with the 3D ILES simulations from this study at $Re = 5.3 \cdot 10^3$ in a jet colormap from blue to red.

After obtaining results simulating a single static NACA0012 airfoil in 2D and 3D at $Re \leq 50 \cdot 10^3$, under a range of α that matched a wide array of experimental data, we surmised that this methodology could be applied to a straight-bladed, low-Re VAWT.

IV. ILES Simulation of low-Reynolds VAWT

The VAWT chosen for this study was the one built and tested by Strickland and reported in [39] as well as in [8]. Since the model VAWT was actually tested in a tow-tank, the average chord Reynolds number for turbine blades is approximately $40 \cdot 10^3$. A schematic of the experimental test setup is shown in Fig. 8. The width of the tow tank was 5 m, so the effect of the side walls on the turbine blades is negligible. However, the bottom of the blades were only approximately 35 cm away from the bottom of the tank, so the proximity of this boundary on the blades could have a significant effect on the flow around the blades. The physical parameters of the VAWT are shown in Table 1. The definitions of these parameters are shown in Fig. 9 where the 2-bladed VAWT is shown in plan view. A plot of the variation of the angle of attack as well as the chord Reynolds number for various tip-speed ratios λ is shown in Fig. 10.

In [39], the authors do not explicitly report the blade offset distance c_0, which is the distance from the leading edge of the airfoil to the blade mounting point, along the chord line of the airfoil. However, from the discussion on pages 57 and 59 of [39] on the measurement of the moment about the quarter-chord, we infer that $c_0 = c/4$. From this section, we also infer that the intended blade offset pitch angle α_0, as shown in Fig. 9, to be $0°$. Yet, the authors report uncertainty in the measurement of the azimuthal angle on the order of $1°$. The determination of the actual α_0 used in the experiments is discussed in Sec. IV C. In the tow tank experiments the forces were averaged over a particular time step, which corresponded to a change of $\theta \approx 15°$. In their numerical simulations, they also encountered a phase shift between the numerical results and the experimental results. In the present study, we found that if we shifted θ of the experimental results by -15° only for λ of 2.5 and 7.5 then we found the best agreement with our numerical results. All of the following plots include this offset in the azimuthal angle for λ of 2.5, 7.5. Unless otherwise noted, the data from the ILES simulations are the averages over all of the passes of the simulations (usually 2 passes for the 3D simulations and 3-4 passes for the 2D simulations) for Blades 1 and 2 at each of the azimuthal positions. In the following sections the sectional tangential force coefficient, C_T is displayed as a function of azimuthal angle θ as defined in 9. The sectional tangential force coefficient is usually

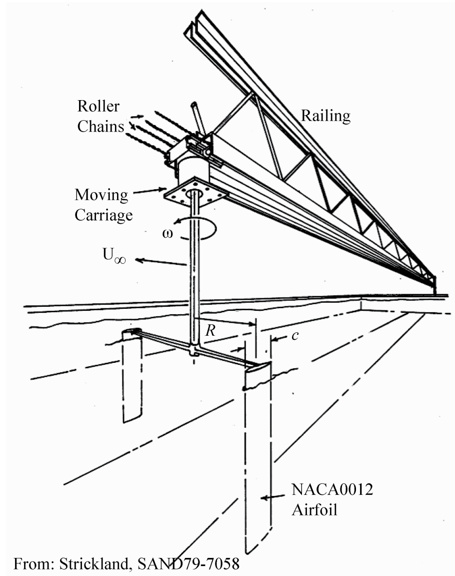

Fig. 8 Schematic of tow tank experiment of low Re VAWT performed by Strickland in [39] and [8].

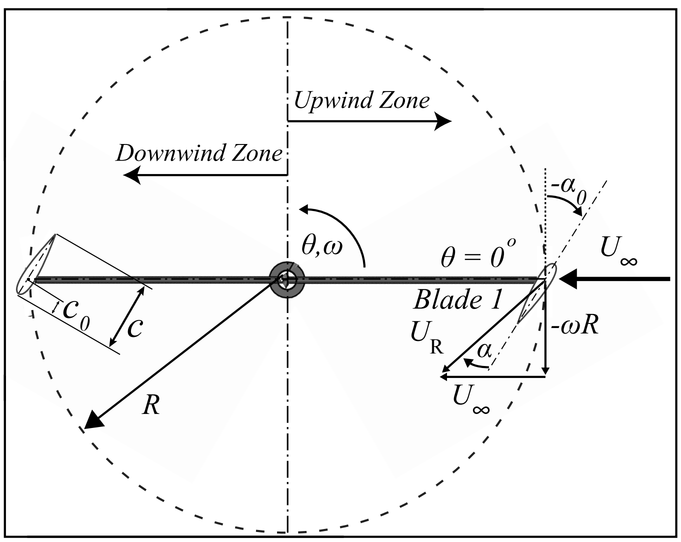

Fig. 9 Plan view of 2-bladed VAWT with definitions of angle of attack α, blade offset pitch angle α_0, chord length c, blade offset distance c_0, VAWT radius R, azimuthal angle θ, and VAWT angular velocity ω.

defined as,

$$C_T = \frac{F_T}{1/2\rho U_\infty^2 c} \tag{1}$$

where F_T is the sectional tangential force on the blade. For a straight-bladed VAWT, the power

Parameter	Value	Unit
c	9.14	cm
R	0.61	m
ω	1.56	rad/s
H	0.85	m
α_0	-2	deg
c_0	0.25c	m

Table 1 Geometry and turbine parameters for the VAWT simulated in this study.

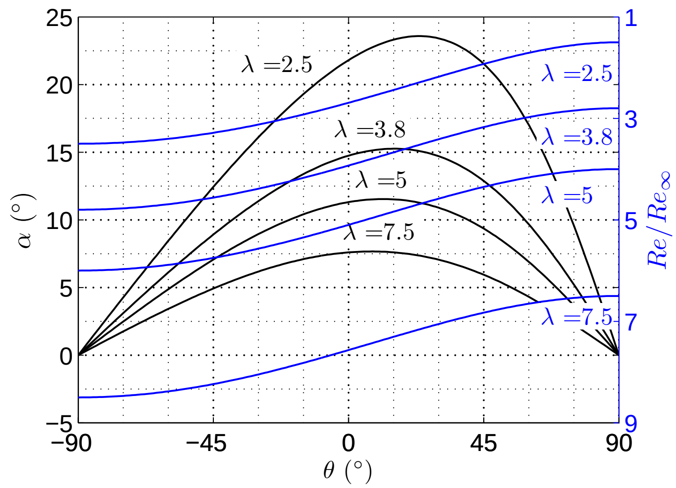

Fig. 10 Variation of angle of attack and chord Re of a straight-bladed VAWT as it completes one half rotation.

coefficient is a function of the average of C_T over one revolution, $\bar{C}_T$ and other parameters, such that

$$C_P = N_b \frac{\frac{\omega}{2\pi}\int_0^{2\pi} F_T(\theta) R d\theta}{1/2\rho U_\infty^3 2R} = N_b \frac{\lambda \bar{C}_T}{2}\frac{c}{R} \qquad (2)$$

A. Computational Domain

The computational domain for the VAWT is shown in Fig. 11. We use a boundary layer similar to the one in the static simulations, and a finer mesh resolution in the near-wake of the airfoils. The 3D mesh is again generation by extruding the 2D mesh, a span of 0.4 chord lengths. The resulting size of the 2D mesh is 11,630 elements, or 116,300 high-order nodes and about 350,000 degrees of freedom. The size of the 3D mesh is 139,560 elements, or about 2.8 million high-order nodes and about 11 million degrees of freedom.

B. Comparison of 2D and 3D ILES

Most of the parameterization study for the ILES simulations were performed in 2D due to the high computational cost of the 3D simulations. In this section, however, we show that the 3D simulations generally follow their 2D counterparts, especially for high TSR. In Fig. 12, the 2D and 3D simulations are compared for $\alpha_0 = -2°$ and $\lambda = 5.0$. Generally, the results of the 2D simulations exhibit the same behavior as the results from 3D cases, albeit with some higher frequency harmonics. In Fig. 13, the results from the 2D and 3D simulations for $\lambda = 2.5$, $T = 25°$ are shown for different α_0. Here, there are discrepancies between the 2D and 3D simulations, especially for $0° \leq \theta \leq 45°$ Thus, we can safely infer that the dominant features that appear in the upwind and downwind zones in the 2D simulations will also appear in the 3D simulations. However, for low TSR, when α is in a post-stall region, the 2D simulations will generally not closely follow their 3D counterparts.

C. Parameterization Study: Pitch Angle Offset

In order to recreate the experiments performed in [8], parameterization studies were performed for the experimental parameters that were not reported or reported with a certain degree of uncertainty. The authors report that discrepancies in the experimental data, *"may be due to misalignment errors in the blade mounting... on the order of* $1°$ *in the blade angle of attack"*. In order to determine the pitch angle offset of the experimental turbine, relatively low-cost 2D ILES simulations were performed for $-5° \leq \alpha_0 \leq +5°$, in increments of $1°$ for $\lambda = 5.0$ and $T = 20°C$. As mentioned previously, the mounting point of the airfoil was taken to be a distance of $c/4$ from the leading edge. The blades were then rotated about this point by an angle of α_0. In these simulations, we found that any toe-in angle ($\alpha_0 > 0°$) of the airfoil decreased the efficiency of the turbine and led to a high variability in blade forces. Thus, in Fig. 14, we only show the tangential force coefficient of the VAWT as a function of the azimuthal angle for $\alpha_0 \geq 0°$ to improve readability. From Fig. 14, it is clear that $\alpha_0 = -3°$, denoted by '+' markers, has the largest maximum value of any of the

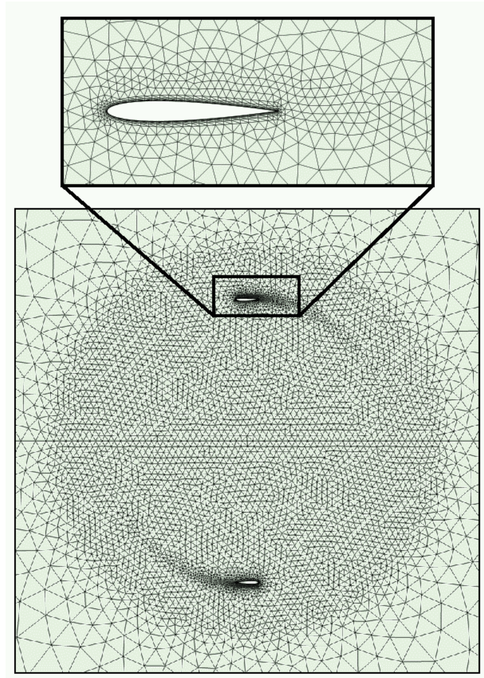

(a) 2D Mesh

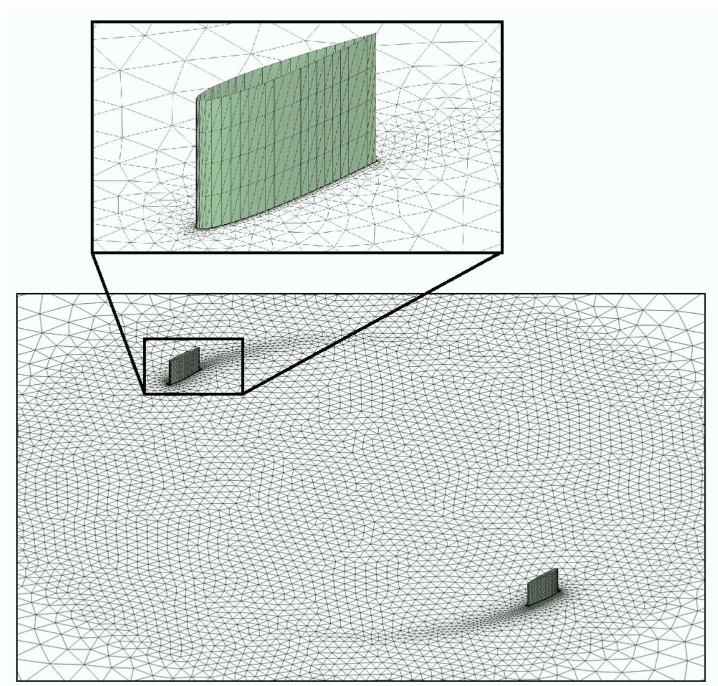

(b) 3D Mesh

Fig. 11 The two high-order computational meshes used for 2D and the 3D simulations of the low Re **VAWT considered in this study. Polynomial degrees of** $p = 3$ **are used within each element.**

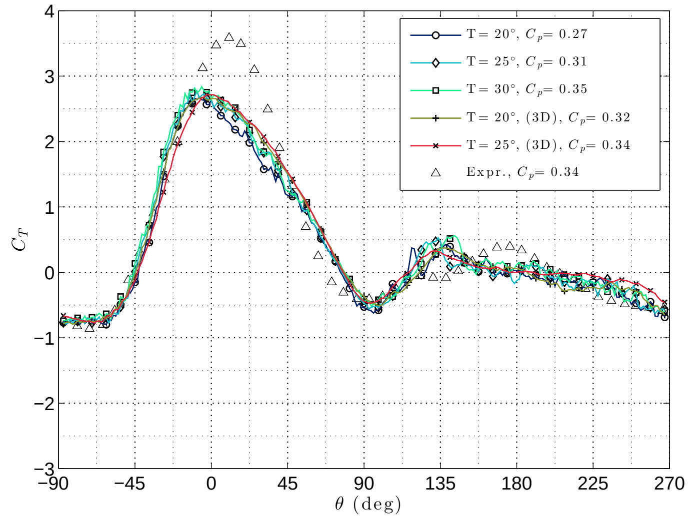

Fig. 12 Tangential force of a VAWT blade as a function of azimuthal position for simulations in 2D and 3D $\alpha_0 = -2^\circ$ at $\lambda = 5.0$ for various temperatures.

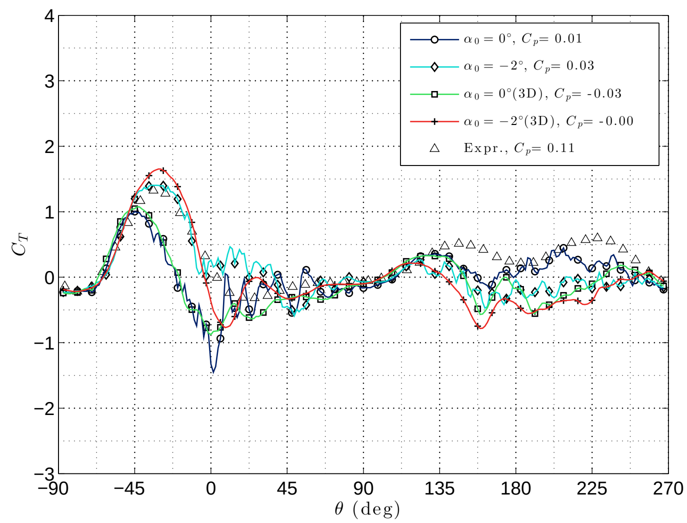

Fig. 13 Tangential force of a VAWT blade as a function of azimuthal position for simulations in 2D and 3D $\alpha_0 = 0, -2^\circ$ at $\lambda = 2.5$.

simulations. However, $\alpha_0 = -2^\circ$, shown with open squares, has the largest power coefficient of the simulations ($C_p = 0.27$). This finding agrees very well with the data collected by Klimas and colleagues for the 5 m VAWT also built and tested by Sandia National Labs [40]. In these tests, which were performed at various λ, the overall maximum power coefficient was achieved for $\alpha_0 = -2^\circ$, ($C_p = 0.32$). Further, this pitch angle offset had the largest C_p for $3.5 \leq \lambda \leq 6.0$.

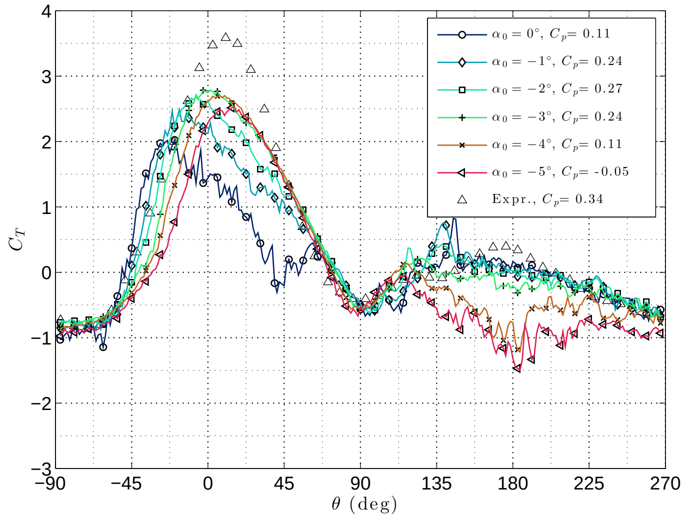

Fig. 14 Tangential force of a VAWT blade as a function of azimuthal position for various α_0 at $T = 20°$, $\lambda = 5.0$

1. Parameterization Study: Temperature of Fluid

After analyzing the ILES simulations of the single NACA airfoil, it became clear that the dynamic fluid structures around the airfoil at high angle of attack were sensitive to the local Re number of the airfoil. Further, the experiments were undertaken at a tow tank at Texas Tech University in Lubbock, Texas, we where the temperature of the fluid could realistically vary by 5-10° depending on the building, insulation, season, etc. We varied the temperature on the order of $5°C$, to slightly change the Re of the flow and examined the numerical results. Though the simulations matched most closely for higher Re (corresponding to higher temperatures), we only thought it was reasonable to assume water temperature of at most $25°C$. The data for the kinematic viscosity of water as function of the temperature was found in [41]. Figure 15 shows the tangential force coefficient as a function of azimuthal angle at $\lambda = 5.0$ and $\alpha_0 = -2°$ for various fluid temperatures $(20, 25, 30°C)$. Clearly, there is not a large change in the trend of the force as the temperature changes by 5° or 10°. However, for these small temperature changes, we were not expecting such a large change in the turbine power coefficient, C_p. Figure 15 shows that a 5° increase in the temperature, which corresponds to a 10% increase in the Re number (due to the change in the kinematic viscosity of water), yields a 5% increase in power production. However, this increase is within the margin of variation of the torque variation from various passes of the turbine of blade.

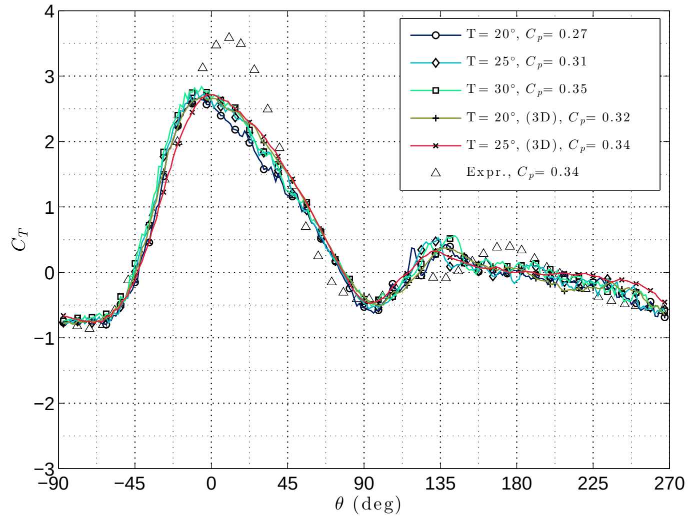

Fig. 15 Tangential force of a VAWT blade as a function of azimuthal position for various T at $\alpha_0 = -2^\circ$ and $\lambda = 5.0$

The 2D results, presented in Fig. 13 show a similar trend but to even a higher degree.

For a wind turbine exposed to environmental conditions the temperature of the fluid cannot be modified. However, this analysis shows that it is critical for researchers to report the temperature of the working fluid in controlled model tests (especially if they are performed in water) so that the conditions can be recreated in such numerical simulations.

D. Comparison with VAWT Analytical Models

Besides simulating the VAWT with ILES methods, two analytical codes were used to estimate the aerodynamic torque on the blades for comparison. A blade-element methodology called the Double Multiple Streamtube Method described in [42] was used along with a dynamic stall model of Berg [43]. This formulation uses a momentum method to model the streamwise wake deficit both in the 'upwind zone' and 'downwind zone' of the rotor (see Fig. 9 for depiction of zones) by iteratively solving for an induction factor. Once this factor is known in the upwind zone for all azimuthal angles, the force on the blades in the downwind zone can be determined. Also, a vortex method developed at Sandia National Laboratories called Code for Axial and Cross-flow TUrbine Simulation (CACTUS) [44] was used to simulate the aerodynamic torque. As of 2013, this numerical method was made available to public as an open-source software [46]. In this model, the data from the twentieth revolution of the turbine was used in order to allow the code to reach a steady-state solution. After corresponding with the authors of the code, the number of blade elements was increased to 10, which slightly improved the accuracy of the code. The sectional lift and drag coefficients for both of the codes came from the experimental data of [23] and [25]. For these codes, the angle of attack was calculated at the mid-chord, as recommended in [8].

The experimental data of the tangential force coefficient shown as triangles in Figs. 16, 17 and 18 was taken as a blade swept over the first half of its fourth revolution (the only tabular data provided in [8]). Due to the computational intensity of the ILES, the data from the ILES 2D and 3D simulations were taken from the forces on 'Blade 2' as it made its first pass from $-90° \leq \theta \leq 270°$ after starting from $\theta(t = 0) = -270°$. However, subsequent revolutions exhibited similar behavior, which was in agreement with the experimental data. The data from CACTUS was taken at 32 instances on the twentieth revolution of the simulation. The DMST only estimates the torque on the blades as an average for a single revolution (no unsteady effects) but the resolution can be increased by increasing the number of streamtubes.

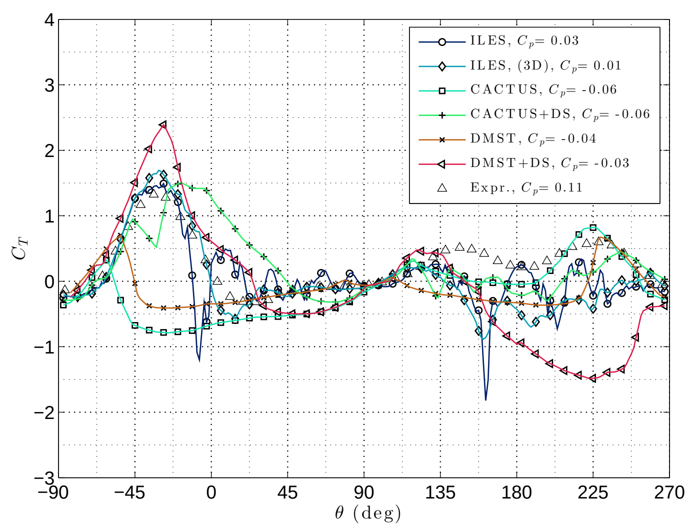

Fig. 16 Tangential force of a VAWT blade as a function of azimuthal position λ=2.5

Figures 16, 17 and 18 show that the ILES simulation can approximate the experimental data very well at high TSR, especially in the downwind section. At λ=2.5, the CACTUS model utilizing the Leishman-Beddos dynamic stall model (described in [45]) recreates the experimental data the best. However, at higher TSR the accuracy of the analytical models drops drastically resulting in

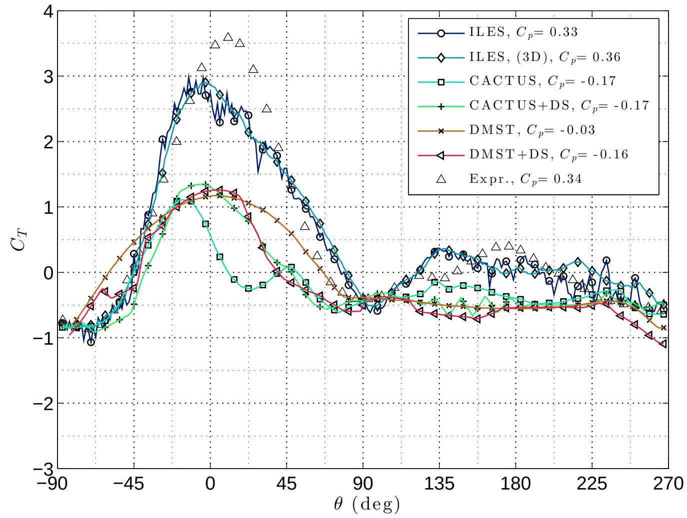

Fig. 17 Tangential force of a VAWT blade on a straight-bladed turbine as a function of azimuthal position for λ=5.0

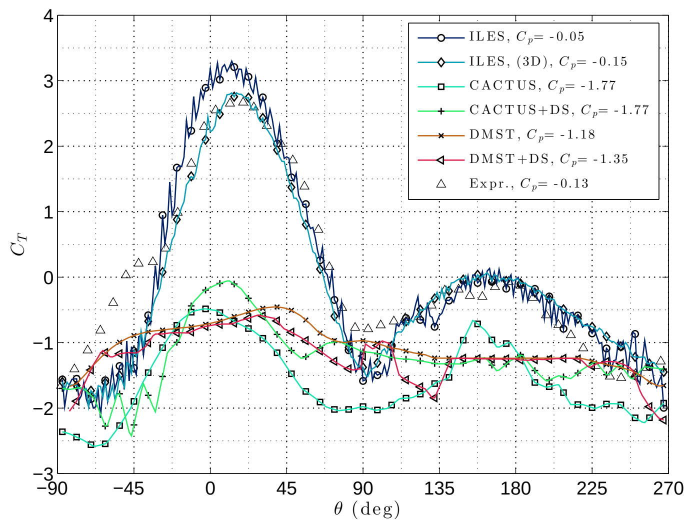

Fig. 18 Tangential force of a VAWT blade as a function of azimuthal position for λ=7.5

highly inaccurate predictions for the power coefficients.

E. Flow Structure

Iso-surfaces of the q-criterion are frequently used to visualize the unsteady 3D flow structures in the fluid domain. The q-criterion physically represents areas where rotation dominates the strain of the flow. In the core of a columnar vortex, $q > 0$ since vorticity increases as the radial distance to the core decreases [11]. In Fig. 19, iso-surfaces of the q-criterion, where $q = 100$, are shown in 3D for various azimuthal angles of Blade 1 when $\lambda = 2.5$. As shown in the top row of Fig. 19, the azimuthal angle θ is $0°$ and columnar vortices are present in the downwind zone of the turbine. These vortices were shed in the wake of Blade 2 from its previous pass and then convected downstream due to the incident wind. The image to the right is a more detailed depiction of the iso-surfaces formed around Blade 1. At this instant in time, the angle of attack α is greater than $20°$, excluding dynamic effects (see Fig. 10). Clearly, there are instantaneous vortical structures forming on the suction side of the airfoil. At $\theta = 60°$ these disturbances have formed into a more coherent structure, labeled 'Vortex A'. The location of Vortex A moves from the upwind zone into the downwind zone due to the influence of the incident wind throughout the time instances in Fig. 19. Interestingly, the vortices are convected too slowly to directly interfere with the flow field around Blade 1 when $120° \leq \theta \leq 180°$.

V. Conclusions

ILES simulations of a single NACA0012 airfoil at large angles of attack as well as a rotating VAWT at a range of TSRs were performed. The results of the single airfoil showed that at pre-stall angles of attack, 2D simulations predicted the lift and drag force well. However, at post-stall angles of attack 3D simulations were necessary as the transverse flow became more important. Further, 3D flow structures in the simulations matched well to PIV and dye-injection experiments. The results from the VAWT simulations showed that the 2D simulations were accurate at high TSR (≥ 5.0). At these TSRs, the maximum angle of attack can exceed $12°$, which corresponds to the post-stall regime. Yet, these 2D simulations, which failed to accurately predict the forces for a static airfoil at these angles of attack, can simulate the forces for the entire turbine fairly accurately. However, these 2D results had high frequency components that were not present in the results from the 3D simulations. From this, we infer that the span-wise length of the airfoil has an averaging effect on the tangential force on the blade. We also confirmed the results of previous researchers that a small toe-out angle can increase the efficiency of the VAWT by nearly 10%. Further, small changes in the viscosity (or temperature) of the fluid can have an influence on the forces on the turbine blades. In the future, we hope to generate longer runs of the 3D VAWT simulations in order to perform

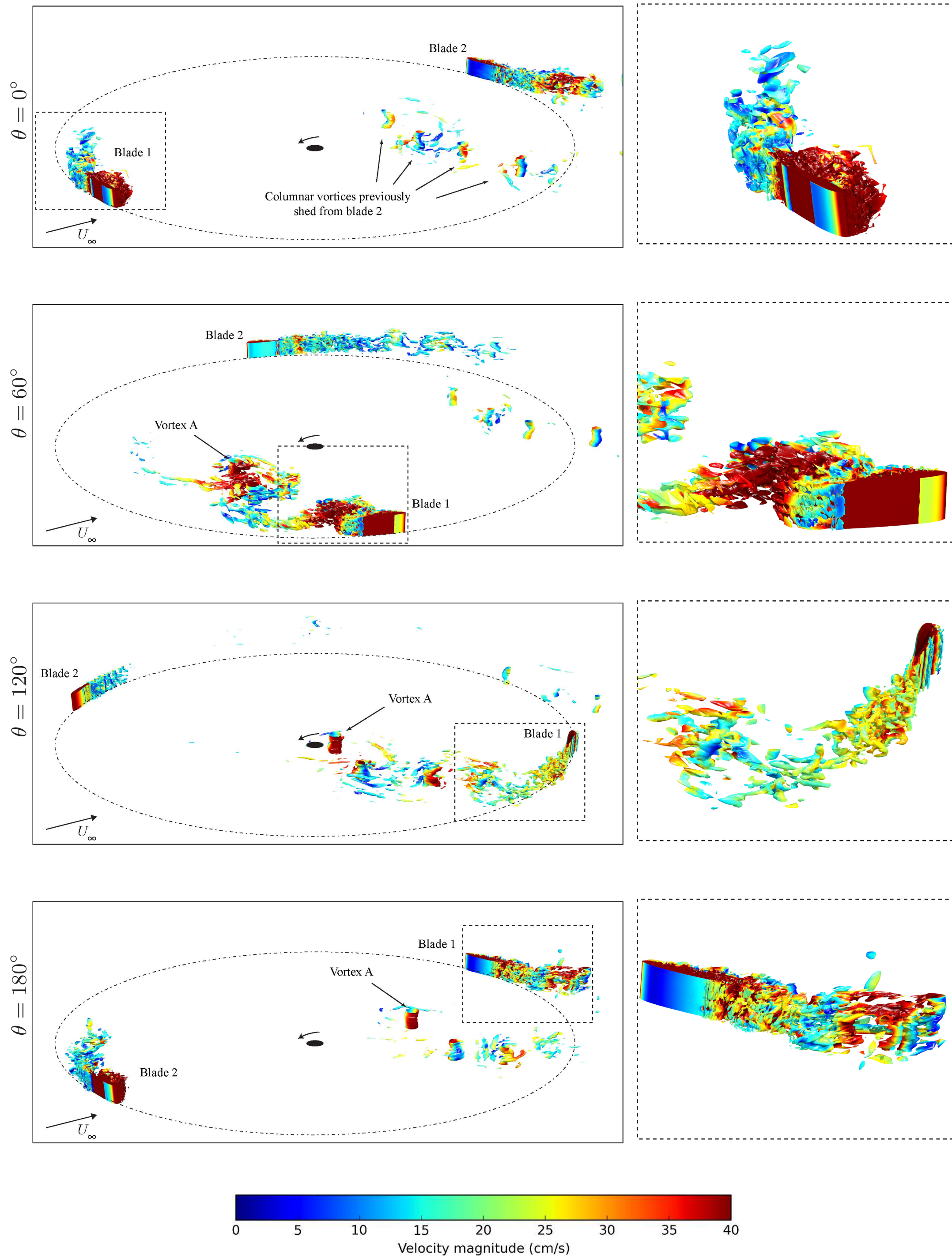

Fig. 19 Iso-surfaces of the q-criterion for $q = 100$ at various azimuthal angles of Blade 1 at $\lambda = 2.5$. Images on right are magnified views of Blade 1. The time evolution of 'Vortex A' is discussed in the text. The isosurfaces are colored according to the magnitude of the velocity, as indicated by the colorbar at the bottom of the figure.

a spectral analysis on the tangential force data. From this analysis, we should be able to estimate the dominant frequencies of the force (of course, 1P and 2P) and at which azimuthal angles they generally occur. Further, we hope to push the Re number of the simulations higher through the use of Detached Eddy simulation (DES) techniques.

Acknowledgements

The first author was supported by the Department of Defense (DoD) through the National Defense Science & Engineering Graduate Fellowship (NDSEG) Program as well as the National Science Foundation (NSF) through the Graduate Research Fellowship Program. The first author would also like to thank Matthew Barone of Sandia National Laboratories for sharing his intuition on simulations of vertical-axis wind turbines. This research used resources of the National Energy Research Scientific Computing Center, a DOE Office of Science User Facility supported by the Office of Science of the U.S. Department of Energy under Contract No. KJ04-01-00-0.

References

[1] D. Roddier, C. Cermelli, A. Aubault, A. Weinstein, WindFloat: A floating foundation for offshore wind turbines, Journal of Renewable and Sustainable Energy 2 (2010) 033104.

[2] H. J. Sutherland, D. E. Berg, T. D. Ashwill, A retrospective of VAWT technology, Sandia National Laboratories (2012).

[3] N. N. SÃÿrensen, J. A. Michelsen, Drag prediction for blades at high angle of attack using CFD, Journal of Solar Energy Engineering 126 (2004) 1011–1016.

[4] H. Gao, H. Hu, Z. J. Wang, Computational study of unsteady flows around dragonfly and smooth airfoils at low reynolds numbers, in: 46th AIAA Aerospace Sciences Meeting and Exhibit, 2008, pp. 7–10. URL: http://arc.aiaa.org/doi/pdf/10.2514/6.2008-385.

[5] C. Li, S. Zhu, Y.-l. Xu, Y. Xiao, 2.5 d large eddy simulation of vertical axis wind turbine in consideration of high angle of attack flow, Renewable energy 51 (2013) 317–330.

[6] J. Smagorinsky, General Circulation Experiments with the Primitive Equations, Monthly Weather Review 91 (1963) 99.

[7] T. J. Mueller, J. D. DeLaurier, Aerodynamics of small vehicles, Annual Review of Fluid Mechanics 35 (2003) 89–111.

[8] J. H. Strickland, T. Smith, K. Sun, Vortex Model of the Darrieus Turbine: An Analytical and Experimental Study. Final Report, Technical Report SAND-81-7017, Sandia National Labs., Albuquerque, NM (USA); Oregon State Univ., Corvallis (USA). Dept. of Mechanical Engineering, 1981. URL: http://www.osti.gov/scitech/biblio/6215602.

[9] P. B. S. Lissaman, Low-reynolds-number airfoils, Annual Review of Fluid Mechanics 15 (1983) 223–239.

[10] B. H. Carmichael, Low Reynolds number airfoil survey, National Aeronautics and Space Administration, Langley Research Center, 1981.

[11] A. Uranga, P.-O. Persson, M. Drela, J. Peraire, Implicit large eddy simulation of transition to turbulence at low reynolds numbers using a discontinuous galerkin method, International Journal for Numerical Methods in Engineering 87 (2011) 232–261.

[12] B. M. Froehle, High-Order Discontinuous Galerkin Fluid-Structure Interaction Methods, Ph.D. thesis, University of California, Berkeley, 2013.

[13] Z. Wang, K. Fidkowski, R. Abgrall, F. Bassi, D. Caraeni, A. Cary, H. Deconinck, R. Hartmann, K. Hillewaert, H. Huynh, N. Kroll, G. May, P.-O. Persson, B. van Leer, M. Visbal, High-order CFD methods: current status and perspective, Internat. J. Numer. Methods Fluids. 72 (2013) 811–845.

[14] P.-O. Persson, J. Bonet, J. Peraire, Discontinuous Galerkin solution of the Navier-Stokes equations on deformable domains, Comput. Methods Appl. Mech. Engrg. 198 (2009) 1585–1595.

[15] J. Peraire, P.-O. Persson, High-order discontinuous Galerkin methods for CFD, in: Adaptive high-order methods in computational fluid dynamics, volume 2 of *Adv. Comput. Fluid Dyn.*, World Sci. Publ., Hackensack, NJ, 2011, pp. 119–152. URL: http://dx.doi.org/10.1142/9789814313193_0005. doi:10.1142/9789814313193_0005.

[16] J. Peraire, P.-O. Persson, The compact discontinuous Galerkin (CDG) method for elliptic problems, SIAM J. Sci. Comput. 30 (2008) 1806–1824.

[17] P.-O. Persson, G. Strang, A simple mesh generator in Matlab, SIAM Rev. 46 (2004) 329–345.

[18] P.-O. Persson, J. Peraire, Curved mesh generation and mesh refinement using Lagrangian solid mechanics, in: 47th AIAA Aerospace Sciences Meeting and Exhibit, Orlando, Florida, 2009. doi:10.2514/6.2009-949, aIAA-2009-949.

[19] W. Shyy, Y. Lian, J. Tang, D. Viieru, H. Liu, Aerodynamics of Low Reynolds Number Flyers, Cambridge University Press, Cambridge, 2007. URL: http://ebooks.cambridge.org/ebook.jsf?bid=CBO9780511551154.

[20] W. J. McCroskey, A Critical Assessment of Wind Tunnel Results for the NACA 0012 Airfoil, Technical Report, 1987.

[21] R. F. Huang, J. Y. Wu, J. H. Jeng, R. C. Chen, Surface flow and vortex shedding of an impulsively started wing, Journal of Fluid Mechanics 441 (2001) 265–292.

[22] R. Huang, C. Lin, Vortex shedding and shear-layer instability of wing at low-reynolds numbers, Aiaa Journal 33 (1995) 1398–1403. WOS:A1995RN90200005.

[23] M. M. Alam, Y. Zhou, H. X. Yang, H. Guo, J. Mi, The ultra-low reynolds number airfoil wake, Experiments in Fluids 48 (2010) 81–103.

[24] S. Yarusevych, P. E. Sullivan, J. G. Kawall, Coherent structures in an airfoil boundary layer and wake at low reynolds numbers, Physics of Fluids (1994-present) 18 (2006) 044101.

[25] T. Ohtake, Y. Nakae, T. Motohashi, Nonlinearity of the aerodynamic characteristics of NACA0012 aerofoil at low reynolds numbers, Japan Society of Aeronautical Space Sciences 55 (2007) 439–445.

[26] O. Lehmkuhl, I. RodrÃŋguez, A. Baez, A. Oliva, C. D. PÃľrez-Segarra, On the large-eddy simulations for the flow around aerodynamic profiles using unstructured grids, Computers & Fluids 84 (2013) 176–189.

[27] M. R. Visbal, R. E. Gordnier, M. C. Galbraith, High-fidelity simulations of moving and flexible airfoils at low reynolds numbers, Experiments in Fluids 46 (2009) 903–922.

[28] M. R. Visbal, High-fidelity simulation of transitional flows past a plunging airfoil, AIAA journal 47 (2009) 2685–2697.

[29] R. Kojima, T. Nonomura, A. Oyama, K. Fujii, Large-eddy simulation of low-reynolds-number flow over thick and thin NACA airfoils, Journal of Aircraft 50 (2013) 187–196.

[30] H. Shan, L. Jiang, C. Liu, Direct numerical simulation of flow separation around a NACA 0012 airfoil, Computers & Fluids 34 (2005) 1096–1114.

[31] M. Breuer, N. JoviÄĎiÄĞ, An LES investigation of the separated flow past an airfoil at high angle of attack, in: Direct and Large-Eddy Simulation IV, Springer, 2001, pp. 165–172. URL: http://link.springer.com/chapter/10.1007/978-94-017-1263-7_20.

[32] I. RodrÃŋguez, O. Lehmkuhl, R. Borrell, A. Oliva, Direct numerical simulation of a NACA0012 in full stall, International Journal of Heat and Fluid Flow 43 (2013) 194–203.

[33] E. V. Laitone, Aerodynamic lift at reynolds numbers below 7 x 10e4, AIAA journal 34 (1996) 1941–1942.

[34] M. Drela, XFOIL: An analysis and design system for low reynolds number airfoils, in: Low Reynolds number aerodynamics, Springer, 1989, pp. 1–12. URL: http://link.springer.com/chapter/10.1007/978-3-642-84010-4_1.

[35] R. F. Huang, H. W. Lee, Effects of freestream turbulence on wing-surface flow and aerodynamic performance, Journal of aircraft 36 (1999) 965–972.

[36] R. E. Sheldahl, P. C. Klimas, Aerodynamic characteristics of seven symmetrical airfoil sections through 180-degree angle of attack for use in aerodynamic analysis of vertical axis wind turbines, Technical Report SAND80-2114, Sandia National Labs., Albuquerque, NM (USA), 1981. URL: http://www.osti.gov/energycitations/product.biblio.jsp?osti_id=6548367.

[37] D. Pagnutti, C. Ollivier-Gooch, Two-dimensional delaunay-based anisotropic mesh adaptation, Engineering with Computers 26 (2010) 407–418.

[38] A. Henderson, J. Ahrens, C. Law, The ParaView Guide, Kitware Clifton Park, NY, 2004.

[39] J. H. Strickland, B. T. Webster, T. Nguyen, Vortex Model of the Darrieus Turbine: An Analytical and Experimental Study., Technical Report SAND-79-7058, Sandia National Labs., Albuquerque, NM (USA); Oregon State Univ., Corvallis (USA). Dept. of Mechanical Engineering, 1979.

[40] P. Klimas, M. H. Worstell, Effects of blade preset pitch/offset on curved-blade darreius vertical-axis wind turbine performance., Technical Report SAND-81-1762, Sandia National Labs., Albuquerque, NM ,USA, 1981.

[41] M. Y. Okiishi, B. Munson, D. Young, Fundamentals of fluid mechanics, John Wiley & Sons, Inc (2006).

[42] I. Paraschivoiu, Wind turbine design: with emphasis on Darrieus concept, Presses inter Polytechnique, 2002.

[43] D. E. Berg, Improved double-multiple streamtube model for the darrieus-type vertical axis wind turbine, in: Presented at the Am. Solar Energy Soc. Meeting, Minneapolis, 1 Jun. 1983, volume 1, 1983. URL: http://adsabs.harvard.edu/abs/1983ases.meet.....B.

[44] M. F. Barone, J. Murray, The development of CACTUS: a wind and marine turbine performance simulation code., Technical Report, Sandia National Laboratories, 2010. URL: http://www.osti.gov/scitech/biblio/1038169.

[45] J. G. Leishman, T. S. Beddoes, A generalised model for airfoil unsteady aerodynamic behaviour and dynamic stall using the indicial method, in: Proceedings of the 42nd Annual Forum of the American Helicopter Society, Washington DC, 1986.

[46] At the time of publication, CACTUS is available at http://energy.sandia.gov/?page_id=16734